From strain to displacement: using deformation to enhance distributed acoustic sensing applications

Alister Trabattoni [1], Francesco Biagioli [2], Claudio Strumia [3], Martijn van den Ende [1], Francesco Scotto di Uccio [3], Gaetano Festa [3], Diane Rivet [1], Anthony Sladen [1], Jean Paul Ampuero [1], Jean-Philippe Métaxian [2] and Éléonore Stutzmann [2]

[1] *Université Côte d'Azur, Observatoire de La Côte d'Azur, CNRS, IRD,, Géoazur, 06560 Valbonne, France.* E-mail: *alister.trabattoni@gmail.com*
[2] *Université Paris Cité, Institut de Physique du Globe de Paris, 75005 Paris, France*
[3] *Università di Napoli Federico II, Dipartimento di Fisica "Ettore Pancini", 80126 Napoli, Italy*

SUMMARY

Over a period of less than a decade, distributed acoustic sensing (DAS) has become a well-established technology in seismology. For historical and practical reasons, DAS manufacturers usually provide instruments that natively record strain (rate) as the principal measurement. While at first glance strain recordings seem related to ground motion waveforms (displacement, velocity and acceleration), not all the seismological tools developed over the past century (e.g. magnitude estimation, seismic beamforming, etc.) can be readily applied to strain data. Notably, the directional sensitivity of DAS is more limited than conventional particle motion sensors, and DAS experiences an increased sensitivity to slow waves, often highly scattered by the subsurface structure and challenging to analyse. To address these issues, several strategies have been already proposed to convert strain rate measurements to particle motion. In this study, we focus on strategies based on a quantity we refer to as 'deformation'. Deformation is defined as the change in length of the cable and is closely related to displacement, yet both quantities differ from one another: deformation is a relative displacement measurement along a curvilinear path. We show that if the geometry of the DAS deployment is made of sufficiently long rectilinear sections, deformation can be used to recover the displacement without the need of additional instruments. We validate this theoretical result using full-waveform simulations and by comparing, on a real data set, the seismic velocity recovered from DAS with that recorded by collocated seismometers. The limitations of this approach are discussed, and two applications are shown: enhancing direct *P*-wave arrivals and simplifying the magnitude estimation of seismic events. Converted displacement provides better sensitivity to high velocity phases, improves broadside response and permits the direct application of conventional seismological tools that are less effective when applied to strain (rate) data.

Key words: Earthquake ground motions; Seismic instruments.

1. INTRODUCTION

In recent days, distributed acoustic sensing (DAS) has rapidly gained traction in the seismological community. The technology is used in a wide range of applications across diverse disciplines. The widespread adoption has been greatly accelerated thanks to the availability of ready-to-use telecom dark fibres, and its sensing capabilities in harsh/underwater environments where regular seismometers would have been difficult to deploy and real-time acquisition would be challenging. The DAS technique typically consist in mea-

suring variations of the phase of backscattered light at each location along an optical fibre to estimate the longitudinal dynamic strain (Hartog 2017). This provides the equivalent of a uniform, dense array of sensors while deploying only one instrument at one end of the cable. For historical and practical reasons, DAS interrogators natively record strain (or strain rate, its temporal derivative), while traditional seismologic instruments record translational ground motions (displacement, velocity or acceleration). Because strain is a spatial derivative of the displacement, it differs from particle motion in several respects. First, strain measurements have a characteristic

directional sensitivity (i.e. a dependence on the direction of propagation and on the particle motion of the recorded wave) with narrower directional sensitivity for *P* waves and a clover-like response pattern for *S* waves (Martin *et al.* 2021). Second, strain measurements are more sensitive to slow waves, amplifying highly scattered waves that are difficult to analyse (Trabattoni *et al.* 2022). And last, finite-gauge length DAS measurements exhibit spectral notches in their instrument response at integer multiples of the apparent phase velocity over gauge length (e.g. Yang *et al.* 2022a). Most of the tools developed in seismology are adapted to translational ground motion measurements, which may require some modification to be used with strain. For instance, magnitude estimation was historically calibrated on the Wood–Anderson seismometer and all magnitude scales require ground displacement inputs. It has also been shown that beamforming can fail on strain data due to the predominance of scattered waves that reduce the wavefield coherence (van den Ende & Ampuero 2021).

For those reasons, several studies have proposed different ways to convert strain to displacement (or other combinations of time derivatives of those two quantities). A first approach is to use the dominant apparent velocity of the observed phases (Daley *et al.* 2016). The reference velocity is generally estimated to correspond to the moveout of the most energetic phases. This approach has been successfully used for magnitude estimation in both offline and real-time early-warning contexts (Lior *et al.* 2021, 2023). The main limitation is, however, that only dominant phases are correctly converted. In particular, the relative amplitude between phases with different apparent velocities remains unmodified. This is problematic when the phases of interest have lower amplitudes than the dominant phases. Exact conversion should rebalance the respective amplitude of phases with different apparent velocities. This is particularly useful to enhance body waves that have a much higher apparent velocity relative to shallow scattered waves (van den Ende & Ampuero 2021).

In this study, we focus on an alternative way to convert strain to ground motion based on numerical integration along the space dimension. FK rescaling (Daley *et al.* 2016; Wang *et al.* 2018; Lindsey *et al.* 2020; Yang *et al.* 2022b) was a commonly adopted first step in this direction. This method allows one to convert strain to velocity by simultaneously integrating in space and differentiating in time in the FK domain. Here, the amplitudes are weighted by the quantity $-\omega/k$, where ω is the pulsation and k the apparent wavenumber along the cable. Because k can be close to zero all studies that used this approach proposed to dampen small wavenumbers to avoid instabilities and the emergence of spurious low-wavenumber signals. These methods are limited to finite 2-D time–space windows, and simultaneously apply a time and a space transformation while sometimes only a space integration would be required (e.g. from strain to displacement or from strain rate to velocity).

Temporal and spatial differentiation/integration can be done separately instead of combining time and space transformation by FK rescaling (note that the FK transformation can be done by applying the Fourier transform twice, in any order, over the time and the space dimensions). We will leave aside the temporal transformation needed to convert strain rate into strain because this problem is the same as converting between displacement, velocity and acceleration, and can be addressed with common methods in the time or spectral domains. The problem of the spatial integration is that the (time-varying) initial value (or the integration constant) is unknown. Van den Ende & Ampuero (2021) showed that by using co-located seismometers as reference, the local particle velocity

can be estimated along rectilinear segments through spatial integration of the recorded strain rate. This method is hence limited to setups where co-located sensors are available. On the other hand, Yang *et al.* (2022a) used a new generation of DAS that can natively record integrated strain rate, hereafter called 'deformation rate'. They observed that integrated measurements show spurious low-wavenumber signals that can empirically be removed by spatial or FK filtering methods.

Fichtner *et al.* (2022) laid down a mathematical foundation that explains the origin of the spurious signals observed in strain-integrated recordings along curvilinear paths. The study focuses on transmission measurements where the pulse emitted at one end of the cable is recorded by a unique sensor at the other end of the cable. This type of measurement is not distributed (i.e. sensitive to the strain at each point of the cable) but integrated (i.e. sensitive to the integrated strain along the cable). The authors show that strain-integrated measurements are mostly insensitive to the displacement wavefield except at very specific locations: at the two extremities of the cable (the relative displacement between the two endpoints is measured) and at each curve or kink of the cable. While this is beneficial for transmission measurements (Marra *et al.* 2018), because it allows to retrieve information along the cable (and not only at the endpoints), the consequences for DAS are not developed.

In this study, the theory of deformation measurements along non-rectilinear cables will be presented. Then concepts will be validated by full-waveform simulations and by comparing DAS recordings with co-located seismometers deployed at the Stromboli volcano (Italy). Finally, two applications will be presented: body wave enhancement in a telecom submarine cable laying offshore on the Chilean margin; and direct magnitude estimation for events recorded by a dedicated cable deployed along the Irpinia fault system (Southern Italy).

2. THEORY

The displacement of a body can be decomposed into a rigid-body displacement component and a deformation component (Fossen 2016). Rigid-body displacement is the translation and rotation of the body as a whole. Deformation is the change in shape/size of the body. DAS is sensitive to the latter but only longitudinally along the cable geometry. In the following, we refer to this curvilinear deformation along the cable as 'deformation', as proposed by Yang *et al.* (2022a). This quantity is then related to usual DAS quantities (e.g. strain) and to seismological ground motion quantities (e.g. displacement).

2.1. DAS natively measures deformation

Let us consider a model fibre-optic cable. Each point of the cable is identified by its curvilinear coordinate s which is the distance at rest $L_0(s)$ from the DAS interrogator $L_0(s) = s$. If ground displacement occurs (e.g. due to the passage of a seismic wave) the distance $L(s, t)$ varies. We define the deformation $\delta(s, t)$ as the variation of that distance compared to the undeformed resting distance:

$$\delta(s, t) \equiv L(s, t) - L_0(s). \tag{1}$$

For small ground motion, deformation is equal to the curvilinear integration of $\varepsilon(s, t)$ the strain component along the cable (Fichtner *et al.* 2022). This latter quantity is equal to the projection along $\boldsymbol{e}(s)$, the cable directional vector, of the curvilinear derivative of the

displacement $\boldsymbol{u}(s, t)$:

$$\delta (s, t) = \int_0^s \varepsilon \left(s', t\right) ds' = \int_0^s \boldsymbol{e}\left(s'\right) \cdot \frac{\partial \boldsymbol{u}}{\partial s'}\left(s', t\right) ds'. \qquad (2)$$

Note that, if not otherwise mentioned, the regular typed symbols are the along-the-cable component of their bold counterparts, and, that when omitted in a sentence, we refer to those projected quantities.

The operating principle of DAS consists in measuring the phase of the backscattered field generated by a laser pulse to measure scatterers' displacements. At rest, the phase of the light backscattered from position s presents a random structure $\phi_0(s)$ due to the small and spatially randomized variations of the optical index of the fibre glass. For a small deformation of the fibre, the optical distances of the heterogeneities relative to the DAS interrogator change, shifting the phase $\phi(s, t)$ as follows (Hartog 2017):

$$\phi (s, t) = \frac{4\pi n \xi}{\lambda} \delta (s, t) + \phi_0 (s), \qquad (3)$$

where n is the effective optic index of the fibre, ξ is the photo-elastic coefficient that relates the deformation of the fibre to changes of its optical index and λ is the central wavelength in the vacuum of the coherent laser pulse. Finally, the coefficient $4\pi = 2 \times 2\pi$ considers the fact that light travels back and forth in the cable and is affected twice by the cable deformation. The unknown $\phi_0(s)$ prevents the recovery of the static deformation. To get rid of this constant, high-pass filtering can be used with a cut-off frequency related to the frequency content of the signal of interest.

More commonly, the temporal derivative of the phase is used to remove the unknown phase reference. It gives the deformation rate $\dot{\delta}(t, s)$:

$$\dot{\phi} (s, t) = \frac{4\pi n \xi}{\lambda} \dot{\delta} (s, t). \qquad (4)$$

Further applying a spatial derivative gives the strain rate $\dot{\varepsilon}(s, t)$ which has the advantage of being a local measurement (see later):

$$\frac{\partial \dot{\phi}}{\partial s} (s, t) = \frac{4\pi n \xi}{\lambda} \dot{\varepsilon} (s, t). \qquad (5)$$

Most modern DAS interrogators use coherent detection techniques and measure phase as a primitive (Hartog 2017). They compute derivatives numerically in contrast to direct detection techniques, where optical interferometric methods are used to make phase comparisons. Spatial differentiation implies a transfer function that is proportional to the wavenumber. This degrades the low wavenumber sensitivity of DAS. Numerical differentiation is also known to produce noisier outputs. Smooth derivative schemes are generally used (e.g. by averaging the derivative over a spatial window). For most DAS interrogators, the user can tune the spatial smoothing through the choice of a parameter called gauge length. This latter quantity damps the high wavenumber signals and can introduce notches to the instrumental response (Yang *et al.* 2022a). This implies that the user can only access to a low-pass version of the deformation and that this limits the reconstruction of signals with short apparent wavelength. This study will not address this technical limitation. We will show that deformation, which is proportional to phase, can be used to directly recover displacement.

2.2. Illustration of deformation recordings

For didactic purpose, we ran a simple numerical simulation (Fig. 1). A synthetic cable deployment is exposed to an incoming impulsive plane P wave made of a 7.5 Hz Ricker wavelet. The medium is homogenous with P-wave velocity of $1\,\mathrm{km\,s^{-1}}$. The geometry of the cable includes perfect and perturbed linear sections, kinks and a curved section (Fig. 1a). It also includes a free-hanging section that is oscillating (e.g. driven by ocean currents; Mata Flores *et al.* 2023a, b). Strain, that was analytically derived from the displacement (Fig. 1g), appears similar to displacement (Fig. 1d), but it is affected by its comparatively high-pass wavenumber response. For cable segments where the waves arrive with an almost normal incidence (e.g. segment BC), and consequently a longer apparent wavelength, record lower amplitudes. Deformation was computed using eq. (7) and curvatures were approximated by an infinitesimal segment-wise rectilinear geometry (see later). Deformation (Fig. 1b) appears as the superposition of the true displacement field (Fig. 1d) and horizontal spurious features (Fig. 1c) that prevent the use of deformation as is for seismic waves analysis. Those features are referred to as 'non-local' effects.

2.3. Non-locality of the deformation

A non-local measurement implies that a measurement made at a given location depends on the value of the field of interest at other locations. Deformation is non-local for two reasons: the lack of a proper reference (referred to as 'reference error') and changes in cable direction (referred to as 'geometric effects').

Let us consider the simple case of a rectilinear geometry (Fig. 2a and segment AB in Fig. 1). Integrating eq. (2) with constant direction $\boldsymbol{e}(s)$ shows that, in this configuration, the deformation is the difference of the displacement $u(s, t)$ between the two integration limits:

$$\delta (s, t) = u (s, t) - u (0, t). \qquad (6)$$

Deformation provides the displacement relative to a reference which is the displacement at the beginning of the cable. If $u(0, t)$ is zero, the deformation is equal to the displacement (Fig. 2c). Otherwise, the motion of the reference point produces a spatially constant (but time-varying) additive term on all measurement points (Fig. 2b). This reference error appears as a space-invariant signal that affects the whole cable (from marker A to F in Fig. 1b).

Along a rectilinear cable, the displacement of one point of the fibre generates an equal amount of positive strain on one side and negative strain on the other side (Fig. 2c). When integrating through, the two contributions cancel out making subsequent measurement points insensitive to the displacement of that point. This is no longer the case when the cable is not rectilinear: the displacement of a point of the cable located at a kink produces an unbalanced amount of strain (Fig. 2d).

For a segment-wise rectilinear geometry, the overall deformation is the sum of the deformation of each rectilinear segment up to the point of interest s. Splitting the integral in eq. (2) per segment and applying eq. (6) per segment, this can be expressed as:

$$\delta (s, t) = u (s, t) - \sum_{k=1}^n \left[u \left(s_k^+, t\right) - u \left(s_k^-, t\right) \right] - u (0, t), \qquad (7)$$

where s_k are the locations of the kinks and n is the number of kinks preceding the location s. At each kink, a new additive constant term appears and impacts all subsequent measurement points. Those terms are equal to the difference between the displacement along the direction before (subscript $-$) and after (subscript $+$) the
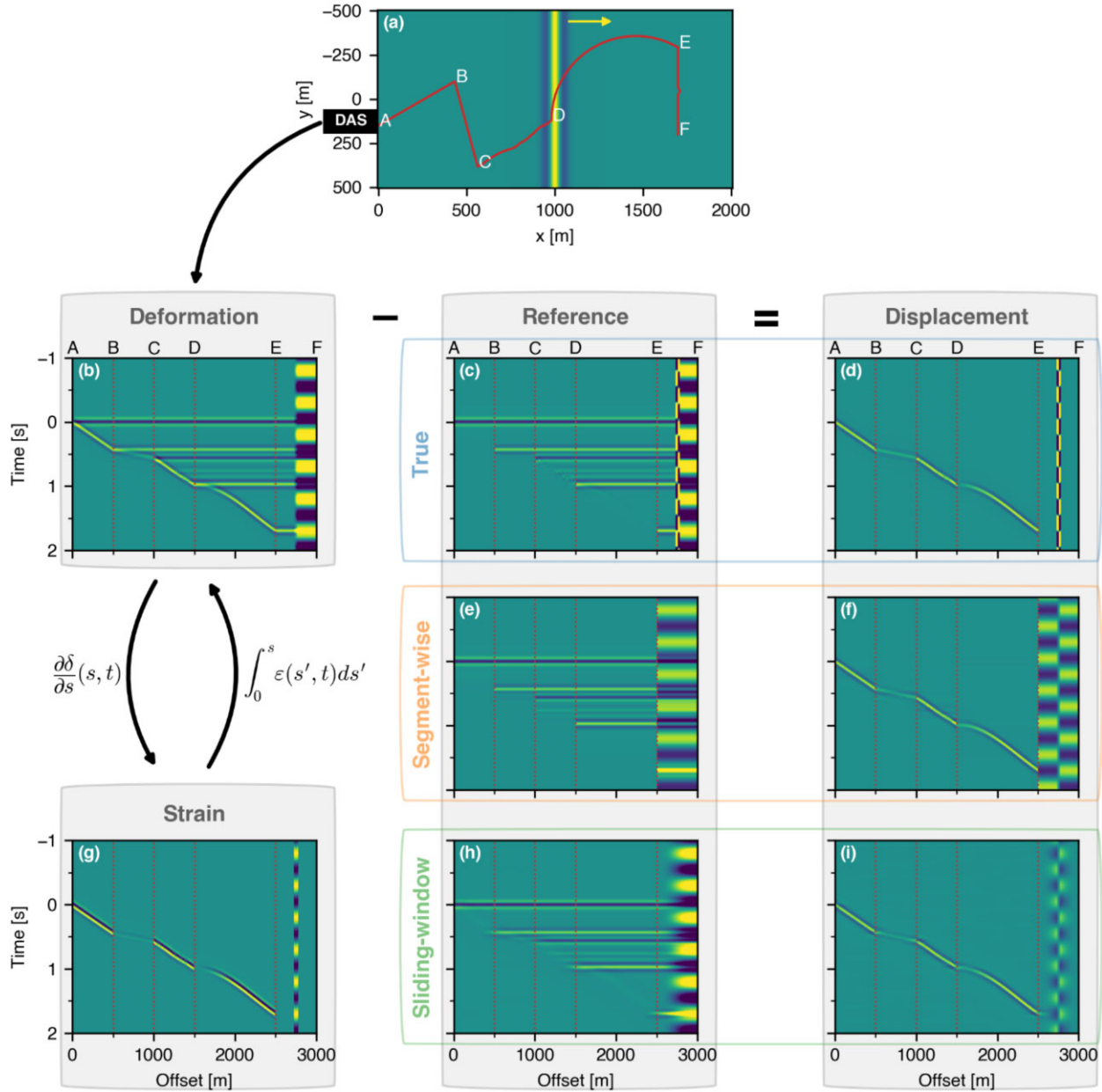
Figure 1. Illustrative simulation. (a) An impulsive plane *P* wave propagating along the *x*-axis produces a horizontal displacement wavefield (blue–green–yellow background raster). A fibre-optic cable (red line) records the deformation along a given geometry. DAS interrogators that use coherent detection techniques measure phase which is closely related to (b) deformation. Deformation is the sum of (d) the true displacement and (c) a reference term (also referred to as 'non-local effects') that must be estimated and removed. Non-local effects can be observed as horizontal features. They are space invariant signals starting at a given offset. The origin is either the beginning of the cable (marker A), a kink (markers B, C, D and E), a perturbation of the rectilinear segment (section CD), the curvature of the cable (section DE), or a nonlinear effect, here produced by a 50-m hanging section at the middle of the segment EF. The simulation was tailored so that non-local effects can be visually distinguished but in general they accumulate an overlap, resulting in data that is difficult to interpret. (f) Segment-wise method: the displacement can be closely recovered, and the locality of the measurement greatly improved by removing (e) the averaged deformation on each segment (red vertical dotted lines). Few horizontal artefacts can be seen (e.g. on segment CD). Sliding-window method: an alternative solution is to remove (h) a sliding average (here 500 m is used with a Hann tapering) to get (i). Artefacts (or border effects) can be observed at some kinks. Spatial differentiation of the deformation gives (g) strain which is a local measurement. Similar results are obtained with an impulsive plane *S* wave (see Fig. S1, Supporting Information).

kinks. It changes the reference against which the displacement is measured. Those geometrical effects appear as horizontal space invariant features that start at each kink location (at markers B, C, D and E, and along the non-rectilinear CD segment in Fig. 1b).

For the general case of a curved cable, it can be shown that integrating eq. (2) by parts (Fichtner *et al.* 2022) gives:

$$\delta(s,t) = u(s,t) - \int_0^s \frac{\partial e}{\partial s}(s')\,u(s',t)\,ds' - u(0,t). \tag{8}$$
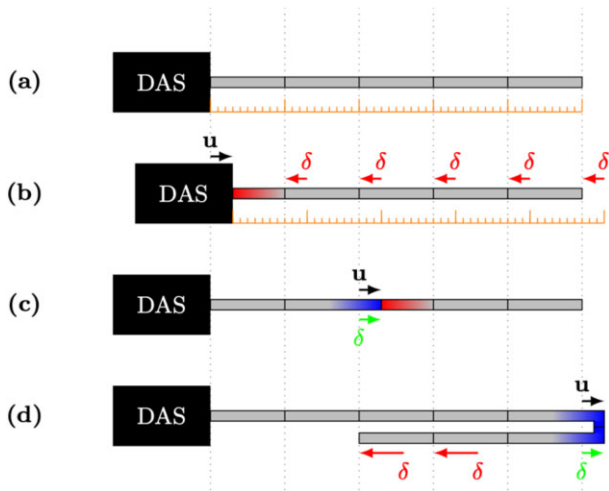
Figure 2. Non-locality of the deformation. (a) A rectilinear fibre-optic cable (grey line) that is at rest. Reference markers (black ticks) are placed at regular distances of the DAS (orange ruler). Let observe three snapshots of the passage of a zero-average localized impulsive wavelet propagating through the cable from left to right. (b) The ground displacement starts to reach the beginning of the cable (blue is elongation and red contraction). The displacement of the instrument produces a contraction of the beginning of the cable that reduces the distance to all subsequent points of the cable. A constant deformation $\delta(s, t) = -u(0, t)$ is added to the entire cable. (c) The deformation is then confined inside the linear section. Because the contraction on one side is equal to the elongation at the other side, the integrated strain cancels out and subsequent points remain unaffected. Since in that case the reference point (the DAS interrogator) also does not move, the measurement is local: $\delta(s, t) = u(s, t)$. (d) Eventually, the impulse reaches the end of the rectilinear section. If the cable continues with a kink (here with a 180° angle), the elongation is no longer compensated by an equal contraction (that here lies outside of the cable). In the case presented here, it is the opposite: the backward part of the kink is elongated with the same amount. The arc length to reach points located after the kink is augmented by twice the displacement of the kink $\delta(s, t) = 2u(s, t)$. This is a typical example of geometric effect showing that integration cannot be applied as is across a kink.

The term $\partial e / \partial s(s)$ represents the sharpness in change of direction. This implies that the radius of curvature plays a central role in the amplitude of this effect (the geometric effect related to the smoothly curved section DE is for example not very pronounced in Fig. 1c).

Non-local effects disappear once spatial differentiation is applied (eq. 5) making strain (rate) a local measurement (Fig. 1g) since every measurement is compared to its neighbours. Next, we show that it is possible to reduce the non-locality of deformation and approximate the displacement by applying suitable processing.

2.4. Recovering displacement from deformation

We have seen that deformation is a measure of displacement relative to a reference that is unknown and related to the displacement of the starting point and the kinks (or curved portions) of the cable. This leads to spurious signals that appear as additive terms which are space-invariant over each rectilinear segment (Fig. 1b). By contrast, seismic signals exhibit a finite wavelength of variation (Fig. 1d) that—if averaged over a sufficiently large length scale—has zero spatial mean. To approximate the non-local effects (Fig. 1c), one solution is then to compute the spatial mean over each rectilinear

segment (Fig. 1e). This estimate of the reference can then be removed from the deformation to estimate the displacement (Fig. 1f). We will refer to this first approach as the 'segment-wise' method. Applying this process to eq. (7) shows that the obtained estimate of the displacement $\hat{u}(s, t)$ is the displacement $u(s, t)$ minus its spatial average $\bar{u}_n(t)$ over the nth segment related to the location s:

$$\hat{u}(s, t) = \delta(s, t) - \bar{\delta}_n(t) = u(s, t) - \bar{u}_n(t). \tag{9}$$

We set as reference the spatial average, essentially replacing an arbitrary reference with one that approximates to zero if the wavelength of the signals of interest is much shorter that the length of the rectilinear section of the cable (see later). The mean can be computed using a weighting (or tapering) window $w_n(s)$ that integrates to one and has zero values outside the nth segment (see later):

$$\bar{\delta}_n(t) = \int w_n(s') \delta(s', t) ds'. \tag{10}$$

Unfortunately, deploying linear sections of cable is often impractical and, in many cases, the user has only limited knowledge on the cable geometry (e.g. for submarine cables). In those cases, a more flexible approach is to choose a characteristic length over which we expect the cable to be approximately linear. Then for each cable location, the reference is estimated by removing a local sliding average (Figs 1g and h):

$$\hat{u}(s, t) = \delta(s, t) - (w * \delta)(s, t) = u(s, t) - (w * u)(s, t), \tag{11}$$

where $*$ denotes the convolution along space and w is a chosen weighting window. This second approach will be referred to as the 'sliding-window' method. To get the values at the ends of the cable, padding is necessary with this approach. Several padding strategies can be used: filling with zeros, with the edge value, or by reflecting values (using mirrored values on the edge). The choice of the padding mode only affects the beginning and the end of the cable and do not appear to have significant consequences. The reflecting mode seemed to generally work better and was used in this study (see later, Fig. S2, Supporting Information).

The two proposed methods reduce the non-locality of the deformation measurements. The segment-wise scheme limits the non-locality to the size of each segment: the value of the displacement at one location of the cable only affects the values measured within its segment. The sliding-window scheme can be assimilated to a finite impulse response (FIR) filtering method. It limits the non-locality to the width of the chosen sliding window. This can be important for example in case of highly corrupted channels (e.g. the hanging cable in Figs 1f and i) that will only impact a finite width of the cable. On the other hand, the use of infinite impulse response (IIR) filters to perform average removal (or equivalently high-pass filtering as in Yang *et al.* 2022a) theoretically spreads those errors indefinitely. In practice, using both methods with matched cut-off wavenumber provides similar results. Comparison of both approaches can be found in the Fig. S3 of the Supporting Information.

2.5. DAS sensitivity to displacement

The displacement that is recovered in the manner described above only approximates the true displacement. In particular, the mean removal affects the low wavenumber response of the recovered displacement. We will focus on the sliding-window method, but similar results can be shown for the segment-wise method. Using the convolution theorem in eq. (11), the sensitivity can be expressed as:

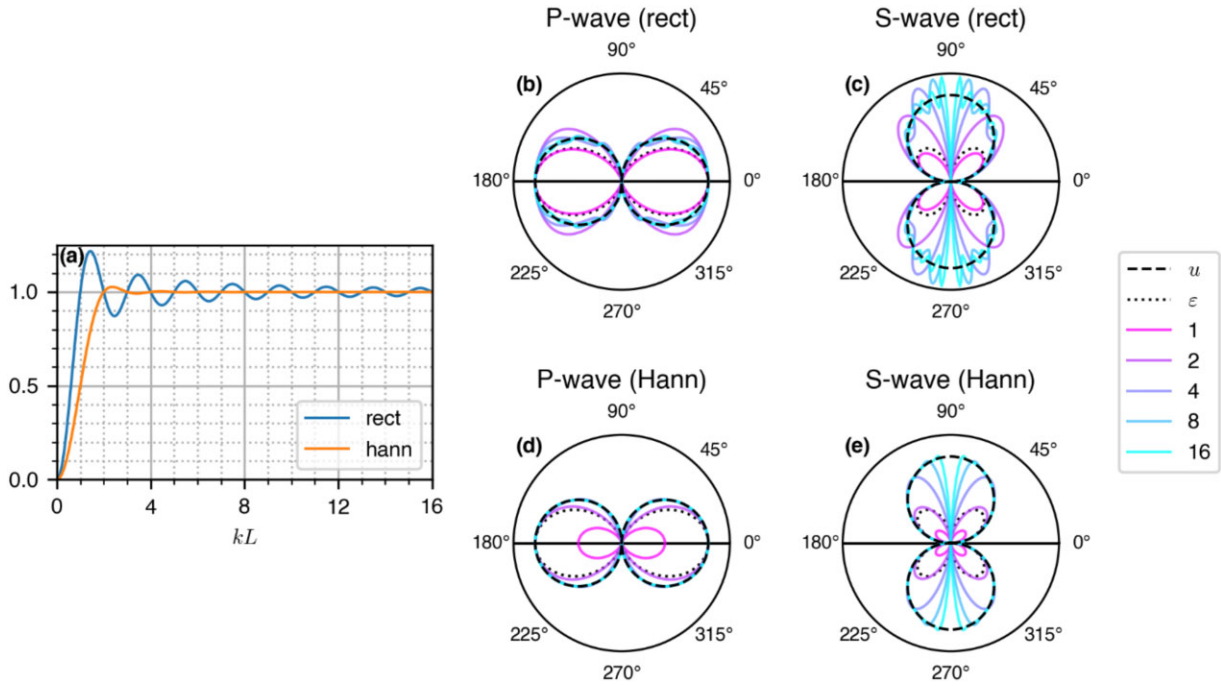$$\hat{U}(k, t) = (1 - W(k)) U(k, t), \tag{12}$$

Figure 3. Sensitivity characteristics of deformation-recovered displacement. (a) The sensitivity is a function of the product between the apparent wavenumber and the length of the rectilinear section (kL); and the shape of the window (here rectangular and Hann windows are shown). Rigid-body displacement cannot be recovered (zero wavenumbers) by DAS. The shape of the window affects the recovered displacement, and its selection requires a compromise between a flat response (no sidelobes) and a strict low cut-off wavelength. Because the apparent wavenumber is a function of the angle of incidence, a directional sensitivity pattern is implied. (b)–(e) Directivity patterns for plane P and S waves for the rectangular and the Hann windows for different kL values (from 1, magenta lines, to 16, cyan lines—see the legend on the right). The horizontal black line indicates the cable direction. For P waves, the sensitivity converges toward the response of the desired displacement (black dashed line) as kL increases. For S waves, waves with orthogonal incidence to the cable have infinite apparent wavelength making their recovery physically impossible. Consequently, the sensitivity of S waves exhibits a notch at orthogonal directions of the cable that gets thinner as kL increases. Note that the rectangular window converges twice faster and has a twice smaller notch than the Hann window, but generates significantly more ripples.

where uppercase letters are the spatially Fourier transformed versions of their lowercase counterparts, and k is the apparent wavenumber along the cable.

Depending on the choice of $w(s)$ the response varies, but some common features are always retrieved. Owing to the relative measurement principle of DAS, rigid-body displacements cannot be recovered. Consequently, displacements of wavelengths that exceed the length of rectilinear sections (approaching the limit of rigid-body translation), cannot be retrieved. On the other hand, wavelengths that are much shorter than the typical rectilinear length tend to average out along the cable length and relative motion of the different parts of the cable can be correctly measured. This mandates the use of long linear segments for studies focused on measuring long apparent wavelengths.

The choice of the optimal weighting function w depends on the nature of the signal and the objective of the analysis. Using a rectangular window implies a sinc weighting function in the wavenumber domain which ensures minimal low wavenumber sensitivity but generates prominent sidelobes (Fig. 3a). The use of a smoother weighting function like the Hann window deteriorates the smallest recoverable wavenumbers but significantly reduces the presence of sidelobes, ensuring a much flatter response (Fig. 3a).

Because the apparent wavenumber depends on the angle of incidence at which the incoming wave strikes the cable, eq. (12) implies a directional sensitivity (Figs 3b–e). Waves orthogonal to the cable have infinite wavelength and cannot be recovered, regardless of their

frequency content. This is already the case for P waves where a single component displacement measurement results in zero sensitivity in the orthogonal direction. For S waves, this produces the presence of a notch whose width depends on the wavelength of interest relatively to the length of the rectilinear section, and on the chosen tapering (Figs 3c and e).

3. VALIDATION

In this section, we validate the proposed displacement (or velocity) recovery method using full waveform simulations, and through comparison with data acquired on the Stromboli volcano by both DAS and co-located seismometers.

3.1. Full-waveform simulation

To evaluate the capacity of DAS to recover velocity instead of the natively provided strain rate, a full-waveform simulation was used to model complex and realistic wavefields. We modelled waves propagating through a shallow sedimentary basin that represents a common situation for DAS deployments both on-land and off-shore. Sedimentary basins produce complex wavefields because ballistic waves are distorted, amplified, trapped and cause interference among each other.

We used the geometry proposed in Trabattoni *et al.* (2022) that corresponds to the case of a dedicated deployment located in the
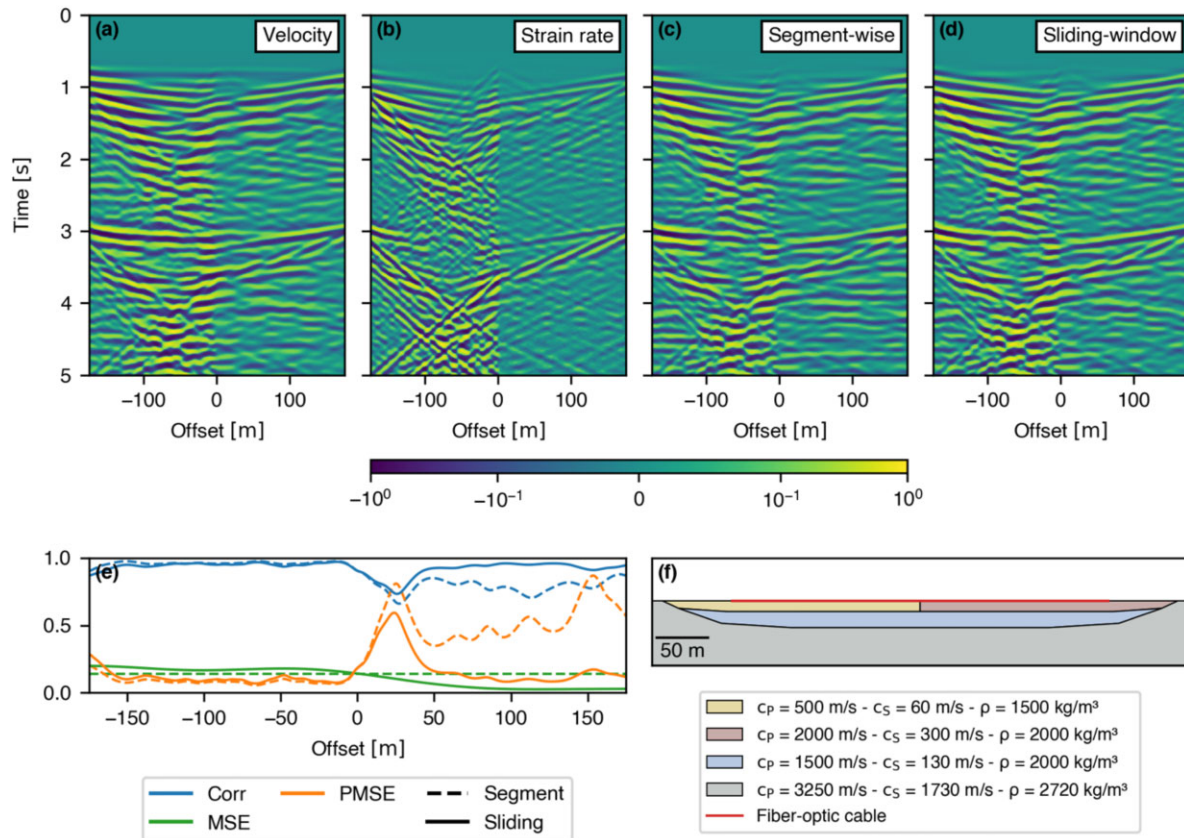
Figure 4. Full-waveform simulation for a shallow sedimentary basin configuration. (a) Simulated particle velocity along the cable. (b) Strain rate along the cable. (c) and (d) Recovered particle velocity along the cable with the segment-wise and the sliding-window methods. While strain rate is almost insensitive to long wavelengths, the phases with high apparent speed are remarkably well reconstructed after the conversion process. Yet, near horizontal arrivals are hardly retrieved since they are associated with high apparent wavelengths, comparable or longer than the fibre extension. (e) Error metrics along the fibre. The error is larger in the higher speed area because waves have inherently longer wavelengths and lower amplitudes. (f) The geometry of the basin, composed of two soft layers superimposed on the bedrock. The speed of the most superficial layer is increased over one half of the basin, to simulate an abrupt wave speed change beneath the cable.

Irpinia Near-Fault Observatory (INFO, Southern Italy). It consists of a two-layer basin of 25 m depth resting on the bedrock (Fig. 4e). To test the influence of shallow heterogeneities beneath the cable, the original model was modified by laterally extending the basin and by including an abrupt lateral change in phase velocity in the upper layer.

We simulated the wave propagation in the basin using SPECFEM2D (Tromp *et al.* 2008). The source consisted of two plane waves (*P* and *S*) with identical angles of incidence (40°) and source time function (5 Hz Ricker) but delayed by 2 s and with different polarities. A 350 m long virtual cable was located at the centre of the basin. The horizontal component of the velocity was evaluated at the surface every 0.5 m with a sampling rate of 200 Hz (Fig. 4a) and used to estimate the deformation (see appendix B), the DAS measured strain rate (Fig. 4b), and the DAS recovered velocity (Figs 4c and d). The latter was obtained using both the segment-wise (eq. 9) and the sliding-window (eq. 11) approaches with the same Hann window whose width was set to the entire length of the cable. Reflection-mode padding was performed to obtain estimates at the cable's extremities (see other padding modes in Fig. S2, Supporting Information).

The velocity wavefield is dominated by high apparent velocity direct and multiple *P* and *S* waves (Fig. 4a). The strain rate wavefield enhances low velocity surface and refracted *S* waves propagating in the basin and increases the amplitude contrast between both sides of the basin (Fig. 4b). Both recovered velocities visually match well with the true velocity. Only the phases with the highest apparent velocities are not perfectly retrieved. The first arrival, which has a particularly high apparent velocity and low energy, is partially recovered especially with the segment-wise approach.

To quantify the error, several metrics were applied at each channel (Fig. 4d): the mean square error (MSE), percentage MSE (PMSE: the MSE divided by the mean square of the reference) and the correlation coefficient (CC). The MSE—which is minimized by mean removal—is constant for the segment-wise approach because the same reference error occurs at each location (i.e. a single reference value is estimated for the entire cable). For the sliding-window approach its value varies with slightly worse results on the high amplitude/low velocity first half of the basin but with much smaller errors in the low amplitude/high velocity section. This result highlights that the segment-wise estimation is driven by the high amplitude areas and that the sliding-window approach better adapts to subsurface wave speed variations. Because of this amplitude contrast, relative metrics (PMSE and CC) better capture the recovery performance. Both the PMSE and CC highlight the difference
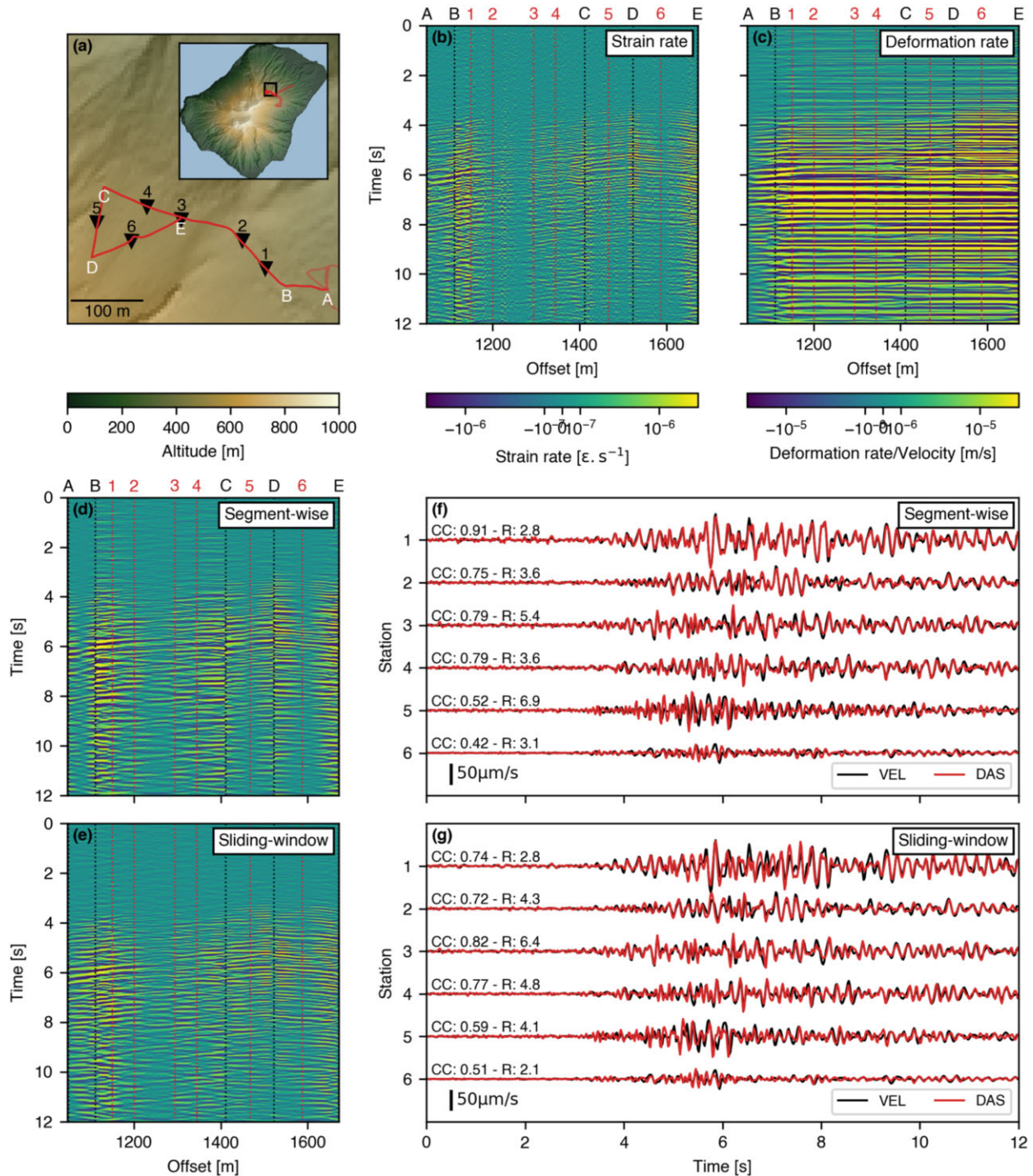
Figure 5. Comparison between velocities recovered from DAS and co-located-seismometers. (a) Deployment of the fibre-optic cable across the northeast flank of Stromboli volcano, with a detail of the fibre section considered in this study (solid red line). Six nodes were deployed (nos 1–6) at the midpoints of the straight segments (black inverted triangles). Letters from A (i.e. the beginning of the cable section) to E (its end) mark the sharp changes in orientation. (b) Strain rate recorded along the considered cable segment. Dashed black lines individuate the changes in cable direction marked in (a). Red dotted lines represent the offsets of the DAS channel closest to each seismometer. (c) Deformation rate without any processing. (d) Velocity recovered with the segment-wise approach using the A-E markers as segment limits. (e) Velocity recovered with the sliding-window approach with a 250 m Hann window. (f) and (g) Comparison between the velocity waveforms from the seismometers (in black) and recovered from DAS (in red), described by means of CC and RMS ratio (R), for the segment-wise and sliding-window approaches, respectively.

between the two approaches but also reveal increased errors at the extremities of the cable and at the location of the subsurface discontinuity. The median CC and PMSE are respectively 0.90 and 20 per cent for the segment-wise scheme and, 0.95 and 11 per cent for the sliding-window scheme. Note that the relative effectiveness of one scheme over the other is scenario-dependent.
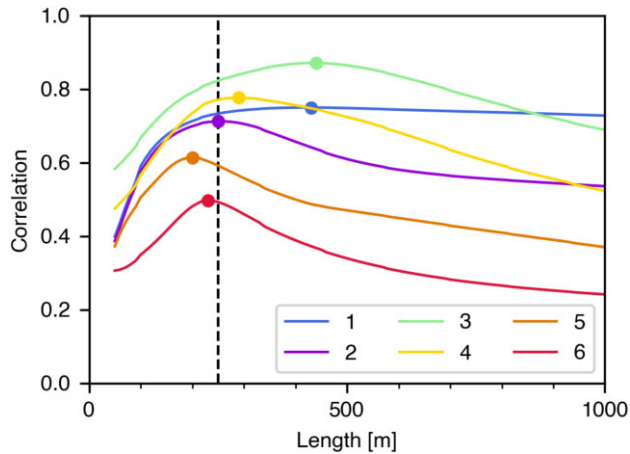
Figure 6. Search of the optimal window length L^*. DAS-recovered velocity computed with different window lengths using the sliding-window approach was compared to the ground velocity recorded at the six co-located seismometers (nos 1–6). The CCs metric was used. Circles mark the optimal values for each channel. We found a correlation between the segment lengths and the value of L^*. Channel no. 5 is located on the smaller segment (DE) and has the smallest L^*. Its L^* is twice its segment length because the effective length of the Hann window is half its size. Channel no. 3 is in the middle of the longest section (BC) and presents the longer L^* of 450 m. The distance to the closest edge seems to be the main factor dictating L^*. A fixed value of 250 m (vertical dashed line) was chosen as the global L^* (Figs 5e and g).

3.2. Comparison with co-located seismometers

To further validate and better illustrate our theoretical developments, we applied our methodology to an experiment with a dedicated fibre-optic cable deployed on the Stromboli volcano. In this experiment, DAS-recovered velocities could be compared with traces recorded by co-located seismometers. A 3 km fibre-optic cable was deployed on the northeast flank of Stromboli to monitor the volcano activity (Biagioli *et al.* submitted). The data presented here was acquired in 2021 September by a Febus A1-R DAS interrogator parametrized with a gauge length of 4.8 m, a differentiation time of 10 ms, a repetition rate of 10 kHz decimated to a sampling rate of 200 Hz and a channel spacing of 2.4 m. This study focuses on a 600 m portion of the cable composed of relatively rectilinear segments where six co-located three-component nodes (SmartSolo IGU-16HR with 5 Hz corner frequency and sampling at 250 Hz) were deployed at the middle of the segments (Fig. 5a). The recordings of an explosive event of mild intensity that occurred at 20:47:03 UTC on 2021 September 26 were studied.

To compare DAS with nodal seismometer data, the recordings were decimated to a common sampling rate (50 Hz) and filtered between 2.5 and 15 Hz (limited by the noise floor of the DAS instrument). The instrumental response of the seismometers was removed and the 3-D particle velocity was projected along the direction of the cable. Strain rate was integrated spatially to get the deformation rate (Fig. 5c). The latter is severely affected by spurious signals which accumulate at each change in cable direction. Velocity was then recovered by applying both the segment-wise (Fig. 5d) and the sliding-window (Fig. 5e) approaches. For the segment-wise approach, the segment limits were manually identified (noted A–E). Because it reduced the recovery performance metrics (see later), one gradual change in the orientation of the cable (between B and C) was not considered as a kink, and the BC segment was treated as a single straight section. This suggests that a compromise between

the segment length and its rectilinearity must be found. For the sliding-window scheme, the choice of the optimal Hann window length (250 m) was estimated by computing, for varying window lengths, the CC between the velocity recovered from DAS and that recorded by the seismometers for each seismometer (Fig. 6). The window length must ideally be longer than the apparent wavelength of the recorded waves and smaller than the characteristic rectilinear length of the cable geometry. Results show that indeed the optimal window length is constrained to the longest rectilinear segment length that can be centred on the channel of interest. Finally, the DAS channels closest to each seismometer (indicated as nos 1–6) were extracted for (Figs 5e and g).

Using either recovery approach, the recovered DAS velocity waveforms exhibit a good agreement in phase with the seismometer recordings. In amplitude, DAS waveforms showed from 2 to 7 times smaller values than seismometer ones, as observed by Biagioli *et al.* (submitted). This was interpreted as imperfect coupling of the cable (implying possible instrument miscalibration). DAS waveforms were individually rescaled to have the same root mean square (RMS) than co-located seismometers ones. For most stations, the CC typically range between 0.7 and 0.8, reaching 0.9 at the station no. 1, with the segment-wise scheme. Two stations underperformed. Station no. 6 was located on a segment featuring a strong bend in the cable made to avoid an outcrop of more competent rock and suffered from strong geometric effects. Station no. 5 was located on the shortest segment (DC) which limited the recovery. Both the sliding-window and segment-wise approaches provides similar results in terms of CC. Looking at the DAS data in space–time plots, the segment-wise approach visibly exhibits space-invariant artefacts (e.g. before the event, close to the borders of the BC segment in Fig. 5d) and wavefield discontinuities at the segment limits (e.g. for the strongest arrival at marker B in Fig. 5d), that arise from the fact that the average is removed simultaneously on all channels and that each segment is treated independently. The performance of the two approaches is comparable. However, the sliding-windows scheme is more flexible and produces fewer space-invariant artefacts.

4. APPLICATIONS

We present two applications illustrating the benefits of converting DAS data using deformation. The first one shows that deformation allows to enhance direct body P waves that are otherwise difficult to observe in strain rate data. The second one shows how magnitude estimation is facilitated using deformation because it permits the use of traditional seismologic methods.

4.1. Direct P-waves enhancement

In and around sedimentary basins (or any subsurface structure covered by soft materials), distributed strain rate measurements are known to be sensitive to site effects and mainly record highly scattered/refracted phases (Trabattoni *et al.* 2022). We will show here that deformation measurements improve the sensitivity to waves with higher apparent speeds and allow one to observe phases that are otherwise indistinguishable.

Sedimentary basins can be found both on land and off-shore. We will focus on a small regional earthquake recorded during a deployment that took place offshore Chile (Fig. 7a). A DAS interrogator (OptoDAS—Alcatel Submarine Networks) was connected in Concón during the month of 2021 November to the submarine fibre optic telecom cable (operated by GTD group) that links Concón
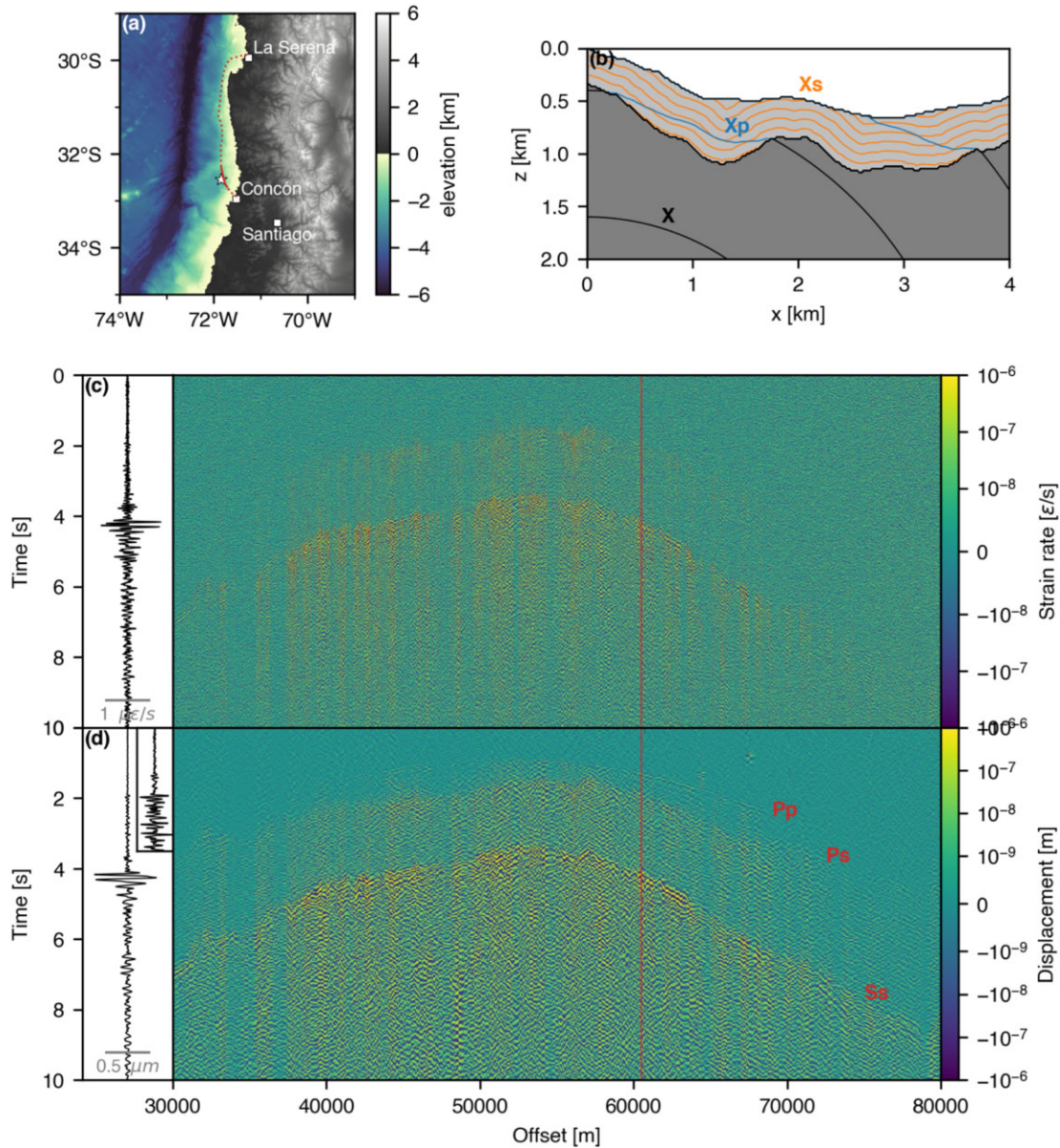
Figure 7. Application of the use of the deformation to recover displacement. (a) Geographic context of the deployment. A submarine telecom cable (dashed red line) was instrumented from Concón. Here only the data coming from the section between 30 and 80 km away from the instrument was used (red solid line) to record a small regional event that occurred very close to the cable (white star: probable location; magnitude was not estimated). (b) Illustration of the strong deformation and amplification of any incoming phase X into a converted/transmitted *S* wave (noted Xs), while the *P* wave (noted Xp) get less distorted. (c) Strain rate. We mainly see the increased high frequency and wavenumber instrumental noise along with slow, strongly scattered waves. On the left inset, the trace of the channel located at offset 61 km (red solid line) is displayed. We mainly see the *Ss* arrival. (d) Displacement recovered using a 1 km sliding Hann window. The noise is reduced, and slow apparent velocity waves are enhanced. This allows for the direct *P*-wave phase (noted Pp) to emerge from the noise. On the left inset, the trace of the channel located at 61 km (red solid line) is displayed. We see three arrivals. A zoom on the first 3.5 s is shown to highlight the *Pp* arrival. Both recordings (strain rate and displacement) have been filtered above 5 Hz to remove the microseismic noise contribution.

to La Serena. A gauge length of 8.16 m was used with a repetition rate of 625 Hz decimated to a sampling rate of 125 Hz and a spatial sampling of 4.08 m.

Both *P* and *S* phases arriving at the bottom of the basin are either converted or transmitted. Because of the very slow velocity of *S* waves in sediments and hence the high *P* to *S* velocity ratio, *S* waves get much more amplified and distorted than *P* waves (Fig. 7b). This results in the dominance of slow refracted/scattered waves. This is further exacerbated for strain rate measurements because of the high sensitivity to slow waves (Fig. 7c). When converting data to

displacement (using the sliding-window scheme with a 1 km Hann window) the increased sensitivity to faster waves allows the observation of faint waves that travel as direct *P* waves in the sediments (Fig. 7d). Also, the overall signal-to-noise ratio (SNR) improves (see Fig. S4, Supporting Information). The enhancement of the direct, coherent *P* arrival potentially enables the use of array processing techniques such as beamforming (van den Ende & Ampuero 2021).

Because the *P*-transmitted *P* arrival (*Pp*) is less distorted, it provides a much better estimate of the *P*-wave arrival time. Studying the arrival time difference between *Pp* and the *P*-converted *S* (*Ps*)
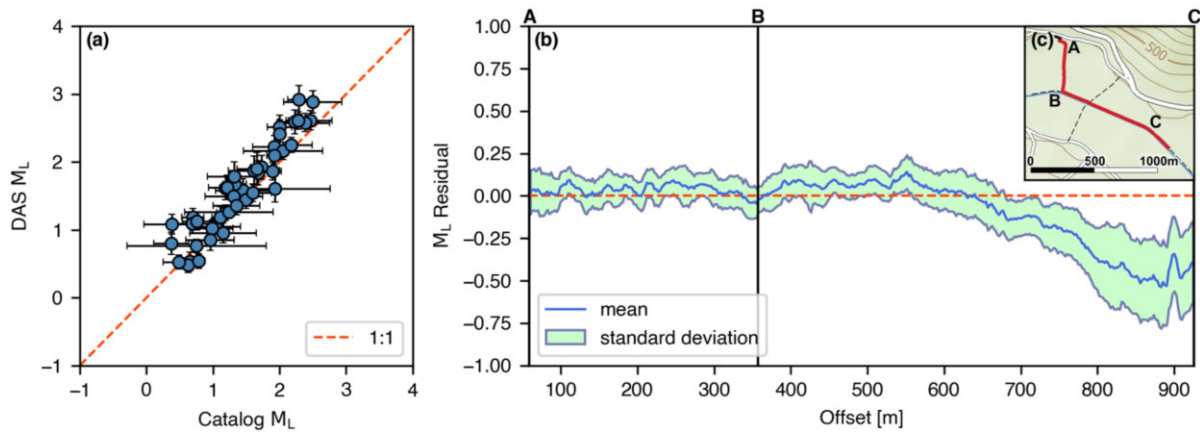
Figure 8. M_L estimation from DAS-recovered velocity. (a) Comparison between DAS and INFO estimates, with associated uncertainties (SMAD). The results are compatible with a 1:1 curve. DAS estimations are slightly overestimated and have lower uncertainty probably because DAS samples a small spatial extent with more correlated hence potentially biased measurements (e.g. due to a common site effect). (b) Mean residual at each channel along the fibre. The curve is represented in between the standard deviation of the residuals. The SNR decreases at the last channels of the fibre, likely due to the influence of the basin structure. The vertical lines represent the separation between the main segments of the Irpinia DAS array, shown in (c). DAS estimations are quite stable along the majority of the cable. The change in the nature of the subsurface between section AB (cultivation field) and BC (dirt road) did not produce any notable magnitude estimation variation.

phases should provide information on the sedimentary structure. Finally, the use of the *Pp* phase should enable more accurate location procedures.

4.2. Magnitude estimation

Most methods that estimate the magnitude of an earthquake rely on the amplitude of particle motion recordings. We propose to use DAS-recovered displacement to directly estimate the local magnitude (M_L) of small earthquakes recorded during the experiment presented in Trabattoni *et al.* (2022). A 1.1 -km long, L-shaped fibre (Fig. 8c) was installed in the active tectonic area of the Southern Apennines (Italy), in the region affected by the 1980 Irpinia *M*6.9 earthquake. It was integrated within the INFO which is composed of 31 permanent seismological stations. The experiment continuously recorded earthquakes and ambient noise for almost five months from 2021 September to 2022 January.

Seismic events were extracted from the DAS records using origin times from the INFO catalogue. Strain rate recordings were filtered between 1–25 Hz, and then converted to deformation rate through spatial integration (eq. 2). The sliding-window scheme was used with a window length of 250 m to recover the velocity. Assuming a flat frequency response for the fibre, velocity traces were transformed into Wood–Anderson displacements by time integration and by applying the specific Wood–Anderson instrumental response. We independently estimated the local magnitude for all the channels along the fibre using the scale tailored for the Irpinia area $M_L = \log_{10} A + 1.79 \log_{10} R - 0.58$ (Bobbio *et al.* 2009). Here, *A* is the maximum peak amplitude of the Wood–Anderson displacement, and *R* is the hypocentre distance (in km).

We selected DAS usable channels according to their SNR, evaluated as the ratio between the maximum amplitude *A* and the RMS of the 20 s period preceding the origin time of the event. Only channels meeting an SNR criterion of 10 were considered. We discarded events with less than 30 channels meeting that criterion, thus reducing the number of usable earthquakes from about one hundred to 44 events. The final magnitude was estimated as the median value of the M_L distribution at all the usable channels $\widetilde{M_L} = \mathrm{median}(M_L(s))$.

To quantify the uncertainties, the standard median absolute deviation (SMAD) over the different available channels was computed as $\mathrm{SMAD}(s) = 1.4826 \times \mathrm{median}(|M_L - \widetilde{M_L}|)$. For comparison, the same process was applied to the traces recorded by the INFO network.

Magnitude estimates provided by the DAS match those computed from the INFO network (Fig. 8a) showing that using DAS recovered velocity enables simple and accurate M_L estimation. This workflow avoids the need of inverting any effective velocity, provides correct magnitude estimation and is computationally efficient.

Looking at the variability of the estimated magnitude along the cable for different events the estimated magnitudes are quite stable for a major part of the cable (Fig. 8b): the estimates of the last segment decrease progressively, maybe due to local site effects and attenuation, for which the calibrated magnitude scale may be inappropriate. This trend could be removed to improve the magnitude estimation.

5. CONCLUSION

While the standard output provided by most DAS interrogators is provided in strain (rate), here we propose to use the deformation (rate) which is the spatial integral of the strain (rate) along the cable. The deformation is closely related to the displacement but presents crucial differences. The key point is that deformation is a measure of the change in length of the cable and provides a displacement measurement relative to a reference. Hence, if the reference is non-zero, the inferred deformation no longer equals the true particle motion at a given location on a DAS cable. As a result, spatially constant offsets appear in the estimated displacement data, and accumulate along the cable. To recover the true displacement from the deformation, with no direct access to a reference (as e.g. provided by co-located seismometers), two methods are proposed. When the cable geometry is known, estimating and removing the spatial mean of the signal for each rectilinear segment effectively eliminates the reference (segment-wise method). In the general case, a sliding average can be used to continuously estimate and remove the reference (sliding-window method). The performance of each

method is comparable, but situationally dependent. Owing to its flexibility and the reduced presence of artifacts we recommend the sliding-widow scheme as the standard conversion procedure.

Displacements recovered from deformation provide an instrumental sensitivity that, compared to strain, presents several benefits: (i) it is compatible with standard seismological tools, (ii) it is more sensitive to long apparent wavelength signals and has a broader directivity pattern and (iii) it is proportional to the phase of the backscattered light which is the primitive measurement provided by most modern DAS interrogators that uses coherent detection techniques hence. On the other hand, deformation-based methods are limited by the rectilinearity of the deployed fibre optic cable. The maximum recoverable wavelength by a rectilinear section is directly linked to its length. This should encourage the use of geometries with long rectilinear segments.

The benefits of deformation-recovered displacement are highlighted for two use cases. It allows direct non-scattered *P* waves with high apparent velocity to emerge for a telecom submarine deployment in a very active subduction context, permitting improved analyses in sedimentary basins context. Furthermore, it allows to use traditional magnitude estimation methods based on DAS data to evaluate the magnitude of small local events using existing attenuation relationships calibrated with a local seismic network; we demonstrated this in an on-land active normal fault context. Because of the low computational cost of the methods, deformation recovered displacement could be used for earthquake early warning. With the proposed data conversion schemes, we bring DAS data closer to traditional seismological data, permitting the reuse of conventional seismological tools.

ACKNOWLEDGMENTS

DATA AVAILABILITY

The data used in this study are available online (https://doi.org/10.5281/zenodo.8152132) along with the scripts used to produce the figures (https://doi.org/10.5281/zenodo.8152229). Analyses were conducted using the xdas python library (https://doi.org/10.5281/zenodo.8152230).

All authors declare that they have no conflicts of interest.

SUPPORTING INFORMATION

Supplementary data are available at *GJI* online.

Figure S1. Same than Fig. 1, but for a plane *S* wave. Similar results are observed meaning that the developed theory applies to both fundamental propagation modes in solids: longitudinal and shear waves.

Figure S2. Effects of different padding modes used in the sliding-window scheme. The true velocity (a) is compared with recovered velocity using: (b) constant zero padding, (c) constant closest value padding and (d) reflection (or mirror) symmetric padding. Results are mostly identical except at the cable ends. (e) Error metrics for each padding mode. The reflect mode has overall better performances for this case.

Figure S3. IIR method taken from Yang *et al.* (2022) and applied to most figures of this study for comparison. A four-order high-pass Butterworth filter can be applied forward and backward along the spatial dimension (resulting in an eight-order filter) to perform an equivalent of the sliding-window method with the same cut-off wavenumber. It works similarly in the sense that the filter is zero-phase and removes low wavenumber components, but some differences can be noted. (h) and (i) Same than Fig. 1. In the illustrative simulation spatial leakage is easily observed and is due to the poor locality of the IIR method. (a) Same than Fig. 3. The response of this method implies a steeper roll-off with lower sensitivity to low apparent wavenumbers compared to the sliding-window method with Hann taper. (b) and (c) This can also be observed on directivity patterns. (d) Same than Fig. 7. On real data, the IIR method gives comparable results. It should be noted that IIR filters are less computationally intensive.

Figure S4. Noise levels of the OptoDAS interrogator. (a) Average raw strain rate levels in the wavenumber domain for 20 s time windows before (noise in blue) and during (signal in orange) the event presented in Fig. 7. (b) Same but for the recovered displacement with a cut-off (vertical dotted grey line) wavelength of 500 m associated with the sliding 1 km Hann window used. (c) Raw strain rate levels but in the frequency domain with a clear cut-off frequency of 5 Hz implied by the filtered meant to remove the microseismic noise. (d) Same for the deformation-recovered displacement. The strain-rate noise level both increases with the wavenumber and the frequency but less than expected (grey dashed line). If noise was an additive white term in deformation and if strain rate was computed by simple spatial and temporal differentiation we would expect linearly. It is probable that other derivation schemes are used, that the noise characteristic in deformation is not white and that more advances proprietary processing technics are used.

Please note: Oxford University Press is not responsible for the content or functionality of any supporting materials supplied by the authors. Any queries (other than missing material) should be directed to the corresponding author for the paper.

REFERENCES

Biagioli, F., Metaxian, J.-P., Stutzmann, E., Ripepe, M., Bernard, P., Trabattoni, A., Longo, R. & Bouin, M.-P., submitted. Array Analysis of Seismo-Volcanic Activity with Distributed Acoustic Sensing. *Geophys. J. Int.*

Bobbio, A., Vassallo, M. & Festa, G., 2009. A local magnitude scale for Southern Italy. *Bull. seism. Soc. Am.,* **99**(4), 2461–2470.

Daley, T.M., Miller, D.E., Dodds, K., Cook, P. & Freifeld, B.M., 2016. Field testing of modular borehole monitoring with simultaneous distributed acoustic sensing and geophone vertical seismic profiles at Citronelle, Alabama: field testing of MBM. *Geophys. Prospect.,* **64**(5), 1318–1334.

Fichtner, A. *et al.*,2022. Theory of phase transmission fibre-optic deformation sensing. *Geophys. J. Int.,* **231**(2), 1031–1039. https://doi.org/10.1093/gji/ggac237.

Fossen, H., 2016. *Structural Geology,* 2nd edn. Cambridge University Press. https://doi.org/10.1017/9781107415096.

Hartog, A.H., 2017. *An Introduction to Distributed Optical Fibre Sensors,* 1st edn. CRC Press. https://doi.org/10.1201/9781315119014.

Lindsey, N.J., Rademacher, H. & Ajo-Franklin, J.B., 2020. On the broadband instrument response of fiber-optic DAS arrays. *J. geophys. Res.: Solid Earth,* **125**(2), https://doi.org/10.1029/2019JB018145.

Lior, I., Rivet, D., Ampuero, J.-P., Sladen, A., Barrientos, S., Sánchez-Olavarría, R., Villarroel Opazo, G.A. & Bustamante Prado, J.A., 2023. Magnitude estimation and ground motion prediction to harness fiber optic distributed acoustic sensing for earthquake early warning. *Sci. Rep.,* **13**(1), 424. https://doi.org/10.1038/s41598-023-27444-3.

Lior, I., Sladen, A., Mercerat, D., Ampuero, J.-P., Rivet, D. & Sambolian, S., 2021. Strain to ground motion conversion of distributed acoustic sensing data for earthquake magnitude and stress drop determination. *Solid Earth,* **12**(6), 1421–1442.

Marra, G. *et al.*, 2018. Ultrastable laser interferometry for earthquake detection with terrestrial and submarine cables. *Science,* **361**(6401), 486–490.

Martin, E.R., Lindsey, N.J., Ajo-Franklin, J.B. & Biondi, B.L., 2021. Introduction to interferometry of fiber-optic strain measurements, in Li, Y., Karrenbach, M. & Ajo-Franklin, J. B., eds, *Geophysical Monograph Series*(1st edn, pp. 111–129). Wiley. https://doi.org/10.1002/9781119521808.ch9.

Mata Flores, D., Mercerat, E.D., Ampuero, J.P., Rivet, D. & Sladen, A. 2023a. Identification of two vibration regimes of underwater fibre optic cables by distributed acoustic sensing. *Geophys. J. Int.,* **234**(2), 1389–1400.

Mata Flores, D., Sladen, A., Ampuero, J., Mercerat, E.D. & Rivet, D. 2023b. Monitoring deep sea currents with seafloor distributed acoustic sensing. *Earth Space Sci.,* **10**(6), e2022EA002723. https://doi.org/10.1029/2022EA002723.

Trabattoni, A., Festa, G., Longo, R., Bernard, P., Plantier, G., Zollo, A. & Strollo, A., 2022. Microseismicity monitoring and site characterization with distributed acoustic sensing (DAS): the case of the Irpinia Fault System (Southern Italy). *J. geophys. Res.: Solid Earth,* **127**(9), https://doi.org/10.1029/2022JB024529.

Tromp, J., Komatitsch, D. & Liu, Q., 2008. Spectral-element and adjoint methods in seismology. *Commun. Comput. Phys.* **3**(1), 1–32.

van den Ende, M.P.A. & Ampuero, J.-P., 2021. Evaluating seismic beam-forming capabilities of distributed acoustic sensing arrays. *Solid Earth,* **12**(4), 915–934.

Wang, H.F., Zeng, X., Miller, D.E., Fratta, D., Feigl, K.L., Thurber, C.H. & Mellors, R.J., 2018. Ground motion response to an ML 4.3 earthquake using co-located distributed acoustic sensing and seismometer arrays. *Geophys. J. Int.,* **213**(3), 2020–2036.

Yang, J., Shragge, J. & Jin, G., 2022a. Filtering strategies for deformation-rate distributed acoustic sensing. *Sensors,* **22**(22), 8777, https://doi.org/10.3390/s22228777.

Yang, Y., Atterholt, J.W., Shen, Z., Muir, J.B., Williams, E.F. & Zhan, Z., 2022b. Sub-kilometer correlation between near-surface structure and ground motion measured with distributed acoustic sensing. *Geophys. Res. Lett.,* **49**(1), 49, https://doi.org/10.1029/2021GL096503.